



Porous carbon directed growth of carbon modified MnO₂ porous spheres for pseudocapacitor applications



Yang Wang^{a, b}, Aiping Fu^b, Xuehua Liu^a, Yiqian Wang^{b, c}, Yanhui Li^b, Peizhi Guo^{a, b, **}, Hongliang Li^{a, b, *}, X.S. Zhao^{a, b, d}

^a Institute of Materials for Energy and Environment, College of Materials Science and Engineering, Qingdao University, Qingdao 266071, China

^b Laboratory of New Fiber Materials and Modern Textile, Growing Basis for State Key Laboratory, Qingdao University, Qingdao 266071, China

^c College of Physics, Qingdao University, No. 308 Ningxia Road, Qingdao, 266071, China

^d School of Chemical Engineering, The University of Queensland, Brisbane, QLD 4074, Australia

ARTICLE INFO

Article history:

Received 15 February 2017

Received in revised form

29 April 2017

Accepted 4 May 2017

Available online 7 May 2017

Keywords:

Spray-drying

Porous carbon

Sacrificial template

Manganese dioxide

Pseudocapacitors

Energy density

ABSTRACT

Carbon modified MnO₂ (CMMO) spheres have been fabricated through a facile low temperature (60 °C) hydrothermal method using mesoporous carbon spheres as reductive agent and sacrificial template and KMnO₄ as manganese source. CMMO spheres with novel nanostructures such as flower-like and sea urchin-like are obtained by controlling the reaction time. The roles of mesoporous carbon in directing the growth of the CMMO spheres and controlling their morphologies have been investigated. The CMMO spheres are characterized by XRD, XPS, SEM, TEM, Raman spectra, TGA and N₂ adsorption-desorption technique and electrochemical measurement. The resulted samples possess unique morphologies and regular pores, and their properties changed as reaction time proceed. The pseudocapacitive behaviors of the as-prepared samples are tested in two-electrode supercapacitors using 2 mol L⁻¹ KOH aqueous solutions as electrolyte. A high gravimetric capacitance of 344 F g⁻¹ at 1 A g⁻¹ and the capacity retaining of 75% after 5000 cycles are achieved on the electrode prepared with one of the CMMO samples. The other CMMO samples also possess excellent electrochemical performance in comparison with the pristine mesoporous carbon (p-MC). Such superior electrochemical performance makes the porous CMMO spheres to be promising materials in the application of pseudocapacitors.

© 2017 Elsevier B.V. All rights reserved.

1. Introduction

Supercapacitors have gained extensive attention in the past few years because of their fast charging time, high power density, long cycle life (>10⁵ cycles), and safe to use [1–7]. However, the energy density of supercapacitors is inferior to that of secondary batteries. As a result, supercapacitors are usually combined with secondary batteries as a supplementary power source [8,9]. Depending on energy storage mechanism, supercapacitors can be classified into two categories: electrochemical double-layer capacitors (EDLCs) and pseudocapacitors [10,11]. EDLCs store charges via a physically

reversible process at the interface of electrolyte and electrode, while pseudocapacitors keep charges through a chemical reaction at the surface of the electrode [12,13]. EDLCs containing carbon-based materials as electrode materials typically deliver a specific capacitance around 150 F g⁻¹ and an energy density less than 10 Wh · kg⁻¹, limiting the application of carbon-based supercapacitors. By comparison, pseudocapacitors with transition metal oxides (e.g. RuO₂, MnO₂, CoO_x, NiO, and Fe₂O₃) or conducting polymers (e.g. polypyrrole, polyaniline, and poly(3,4-ethylenedioxythiophene)) as the electrode materials can provide superior specific capacitance and energy density [14–18].

The theoretical specific capacitance of transition metal oxides can be very high (e.g. RuO₂ > 1000 F g⁻¹) [15]. However, the rate capability and cycling performance of pristine transition metal oxides are poor because of their low electrical conductivity [19]. Therefore, research has been focusing on transition-metal-oxide-based composite materials, which possess outstanding rate capability, high power and energy density [20,21]. Among various metal

* Corresponding author. Institute of Materials for Energy and Environment, College of Materials Science and Engineering, Qingdao University, Qingdao 266071, China.

** Corresponding author. Institute of Materials for Energy and Environment, College of Materials Science and Engineering, Qingdao University, Qingdao 266071, China.

E-mail addresses: pzguo@qdu.edu.cn (P. Guo), lhl@qdu.edu.cn (H. Li).

oxides, manganese dioxide exhibits several remarkable characteristics, such as high theoretical capacitance ($>1370 \text{ F g}^{-1}$) [1,22–26], high abundance in nature, and low cost [1,3,4,15,27]. However, the application of MnO_2 has been seriously restricted by its low electrical conductivity (10^{-5} to $10^{-6} \text{ S cm}^{-1}$) [28,29] and structure instability against cycling [15,30]. To address these problems, researchers have used carbon to modify MnO_2 . Carbon in different phase states i.e. amorphous carbon, graphitic carbon and graphene have been explored for such a purpose [31]. MnO_2 /carbon composites with different combination states and different ratios between MnO_2 and carbon have been fabricated, and most of them show improved capacitive properties than the pristine MnO_2 [15,32]. In most of the cases, carbon materials with high specific surface area were utilized as conductive substrates for MnO_2 particles. Meanwhile, MnO_2 were synthesized by reducing KMnO_4 with reductive agent, e.g. Mn^{2+} salts and other kinds of organic species [33,34]. Carbon substrates themselves can also act as reductive agent and MnO_2 then is deposited on the surface of the substrates in-situ [35]. Normally, the loading content of MnO_2 is restricted in the composites, which will then influence the capacitive properties of the resulted composites.

In this paper, we report a new route that combines spray-drying technique with a low temperature hydrothermal method to the preparation of carbon modified MnO_2 (CMMO) spheres for high performance supercapacitors. Mesoporous carbon (MC) spheres with uniform pore size and relative high specific surface area are prepared via a spray-drying assisted hard template method using chitosan as carbon precursor and SiO_2 nanopaticles as hard template. The resulted MC spheres are then used as reductive agent and sacrificial template for growing carbon modified MnO_2 microspheres by a one-step low temperature hydrothermal process. The formation mechanism of the CMMO spheres has been studied. The resultant CMMO spheres are adopted as electrode materials for pseudocapacitors, and their capacitive performance in 2 mol L^{-1} KOH electrolyte has been investigated. The influences of hydrothermal treatment time on the morphology and electrochemical performance of the resultant CMMO spheres as supercapacitor electrode have also been investigated in details.

2. Experiment section

2.1. Chemical reagents and materials

All chemical reagents including chitosan, acetic acid, hydrofluoric acid, potassium permanganate, potassium hydroxide, sulfuric acid, isopropyl alcohol and alcohol are of analytical grade and purchased from Sinopharm Chemical Reagent Company. HF (40%) and Polytetrafluoroethylene latex (PTFE, 60 wt%) were purchased from Aldrich, while acetylene black (99.99%) were purchased from Strem Chemicals. LUDOX[®] HS-40 colloidal SiO_2 (30 wt%) was procured from Chengsong (Shanghai) International Trade Co., Ltd. Deionized water was used in the experiments.

2.2. Preparation of mesoporous carbon (MC) spheres

The MC spheres were prepared via a spray drying assisted hard template method [36]. In the preparation, chitosan was used as carbon precursor and nanosized SiO_2 particles as hard template. A laboratory-scale SP-1500 spray dryer was utilized for the spray-drying process (Shanghai SunYi Tech Co., Ltd.). In a typical batch, 2 g of chitosan was dissolved in 100 mL of 5% acetic acid aqueous solution, and then 4 mL of a Ludox SiO_2 suspension (30 wt%) was added into the chitosan aqueous solution followed by a 12 h agitation to get a transparent suspension. Then, the suspension was dried by the spray dryer at 160°C with hot air as the carrier gas. The

chitosan/silica composite collected by a cyclone separator was thermally treated in a tube furnace at 400°C for 3 h, followed by at 800°C for 3 h under a high-purity nitrogen flow. Finally, the composite derived from the thermal treatment was dispersed into a 20% HF aqueous solution for 24 h at ambient temperature to etch away the silica. Black solid was collected by centrifugation and washed with deionized water and ethanol for several times, and then the solid was dried at 70°C for 24 h in air to obtain MC spheres.

2.3. Preparation of carbon modified MnO_2 (CMMO) spheres

The CMMO spheres were prepared by using a one-step low temperature hydrothermal synthesis method. In brief, KMnO_4 (0.6 g) and MC (0.04 g) were dispersed to deionized water (50 mL) under stirring. After 12 h, 2 mL of 98% H_2SO_4 was added to the suspension still under stirring for 2 h. Then, the suspension was transferred into a 100 mL Teflon-lined autoclave to be hydrothermally treated at 60°C for different times to obtain samples designated as CMMO-X (where X = 5, 8, 10 and 12 h, standing for the hydrothermal treatment time).

2.4. Characterization

X-ray diffraction (XRD) patterns of samples were collected on a Rigaku Ultima IV X-ray diffractometer with $\text{Cu-K}\alpha$ radiation ($\lambda = 0.15418 \text{ nm}$). Raman spectra were collected on a Renishaw inVia Plus Micro-Raman spectroscopy system equipped with a 50 mW DPSS laser at 532 nm. Nitrogen adsorption-desorption isotherms were measured using a Quantachrome Autosorb-IQ-MP/XR. The specific surface areas of samples were estimated using the Brunauer-Emmett-Teller (BET) method with N_2 adsorption data in the relative pressure range of $P/P_0 = 0.05\text{--}0.35$. Pore size distributions were computed using the Barrett-Joyner-Halenda (BJH) model with the desorption branch data. The thermogravimetric analysis was performed with a Mettler Toledo TGA-2 thermal gravimetric analyzer under an oxygen atmosphere with a heating rate of $10^\circ\text{C}\cdot\text{min}^{-1}$. The morphologies and the structures of the samples were examined by a JEOL JSM-7800F field emission scanning electron microscope (FESEM) and a JEOL JEM-2100 Plus transmission electron microscope (TEM). XPS data were accumulated on an AXIS HS (Kratos Analytical) electron spectrometer system with a monochromatized $\text{Al K}\alpha$ standard X-ray source and the binding energies were calibrated by referencing the $\text{C}1s$ to 285.0 eV.

2.5. Electrochemical measurement

The working electrodes were prepared by mixing the active materials, conductive acetylene black and polytetrafluoroethylene (PTFE) in a mass ratio of 85:10:5. Then a certain volume of isopropyl alcohol was added to gain a uniform suspension. After the partial evaporation of the isopropyl alcohol, the slurry was coated on a nickel foam current collector uniformly, which was then dried at 110°C for 10 h in a vacuum oven. Thereafter, it was compressed into a wafer by a tablet machine and subsequently punched into the working electrode of about 1 cm diameter. Then, The working electrode was weighted, after deducting the mass of collector without active materials, the mass loading density of active materials was calculated to be about 3 mg cm^{-2} . A Teflon-lined home-made cell of stainless steel with inner diameter of 1.2 cm was utilized as prototype for the measurements of electrochemical properties of the CMMO-X samples (A photograph of the cell and its working model please refer Scheme S1). A two-electrode system was assembled with this working model under room temperature

using 2 mol L⁻¹ KOH aqueous solution as electrolyte and a porous membrane as separator. The electrochemical measurements including cyclic voltammetric (CV), galvanostatic charge-discharge (GCD) and electrochemical impedance spectroscopy (EIS) were carried out on a CHI 760D electrochemical workstation (CHI Instruments, China) at different scan rates and current densities.

3. Results and discussion

Fig. 1 (a) shows the XRD patterns of the CMMO-X spheres derived from different hydrothermal reaction times. From the pattern one can find that the sample obtained in a treating time of 5 h shows a broad diffraction peak at around $2\theta = 24^\circ$, indicating an amorphous state of carbon [37]. Another two weak peaks at 37.5° and 65.1° can be indexed to the (211) and (002) crystal planes of tetragonal α -MnO₂. When the time was lengthened to 8 and 10 h, the broad peak at around $2\theta = 24^\circ$ disappeared gradually, and the intensity of other diffraction peaks turn to higher. While the treating time was extended to 12 h, the XRD patterns of the resulted composites conform well to crystalline MnO₂ (JCPDS, NO.44-0141). Fig. 1 (b) shows the TGA curves of four CMMO-X samples, from which one can deduce their thermal decomposition properties. It can be seen that there are three main regions in the curves. A gradual decrease of weight mass below 300 °C has been found, which can be ascribed to the removal of physically adsorbed moistures and the crystal waters. It can be seen that the contents of water decrease from 10.5 to 7.5% with the increase of hydrothermal treating time. The weight loss in the temperature range of 300–560 °C should be attributed to the consumption of the residual carbon. Interestingly, all these samples show quite similar carbon content of about 3.5 wt%. The further slight loss above 560 °C can be explained as due to the phase transformation of MnO₂ to a more stable state of Mn₂O₃ (as shown in Fig. 1(c)) [15,38]. Finally, the content of MnO₂ could be calculated by deducting the weight of water and MC, and the phase transformation of MnO₂ to

Mn₂O₃. Values for the four different samples are of 85.1%, 86.8%, 88.2% and 88.7%, respectively have been calculated. The high content of MnO₂ in these CMMO spheres can be attributed to the porous structure of MC, which made the contact and reaction between permanganate ions and MC more efficient and then resulted in high efficient consumption of MC [15]. Raman spectroscopy was adopted to analyze the specific structures of these samples and the resultant spectra are showed in Fig. 1 (d). The weak D band at 1369 cm⁻¹ can be attributed to the disorder properties of MC, and the G band at 1597 cm⁻¹ originates from the sp² hybridization of C–C bonds [38]. The ratio of the intensity between D band and G band increased from 1.00 to 1.13 with the reaction time extended. Such a result might be ascribed to the corrosion of carbon with KMnO₄ as the reaction time turns longer. More importantly, there are three typical Raman scattering bands of MnO₂ at 510, 577 and 629 cm⁻¹ which are matching well with the Mn–O stretching vibration of MnO₆ octahedral [27,39].

The chemical composition of CMMO-8 composite was further investigated by X-ray photoelectron spectroscopy (XPS). Signals of C, O, Mn and K elements are observable from the full survey (see Fig. 2(a)). Fig. 2(b) shows the high resolution survey at the C 1s region, and from the survey it can be seen that there are three peaks in the spectra. The main peak centered at 284.8 eV can be ascribed to the vibration of C–C and C=O bonds. The intensity of the other two peaks located at 286.4 and 288.5 eV are weaker than the former one, and they correspond to the C=O and C–O bonds, respectively.

Analogously, the high resolution survey at O1s region can be deconvoluted into three peaks situated at 529.6, 531.2 and 533.0 eV (Fig. 2(c)), which are corresponding to the vibration of Mn–O–Mn, Mn–O–H and C–O/C=C, respectively. The core level of Mn 2p region was given in Fig. 2(d). Obviously, there are two main peaks at 641.9 and 653.5 eV, respectively. The spin energy separation of 11.6 eV primely confirms the formation of MnO₂ in the CMMO-X composite, which is in accordance with the documented

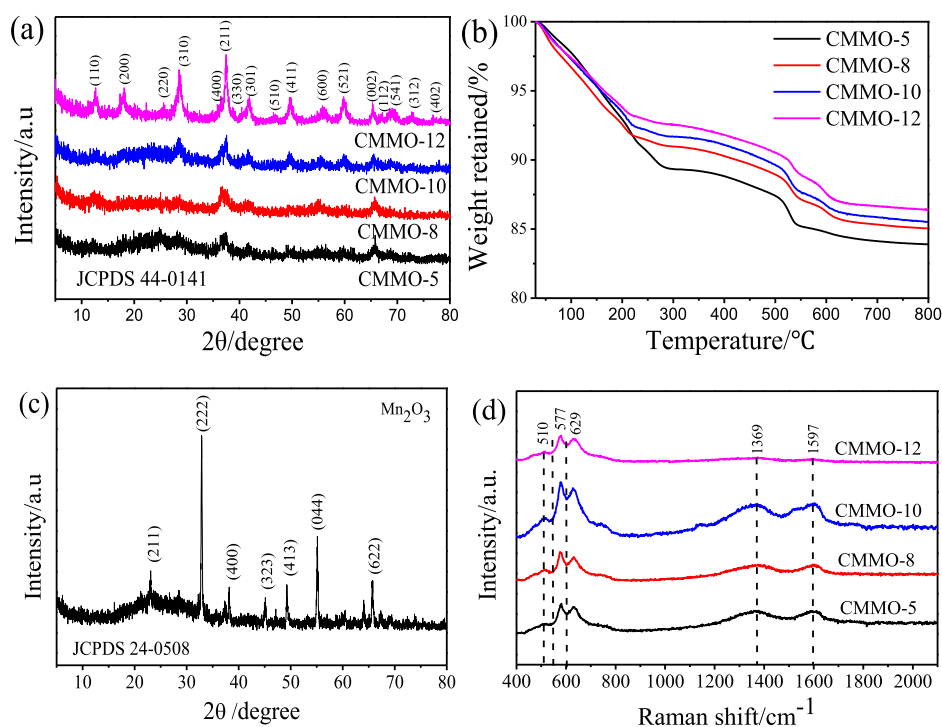


Fig. 1. (a) XRD patterns of CMMO-X; (b) thermogravimetric analysis (TGA) curves of CMMO-X; (c) XRD patterns of the corresponding product (Mn₂O₃) after thermal treatment of CMMO-8 at 800 °C in air atmosphere; (d) Raman spectra of CMMO-X.

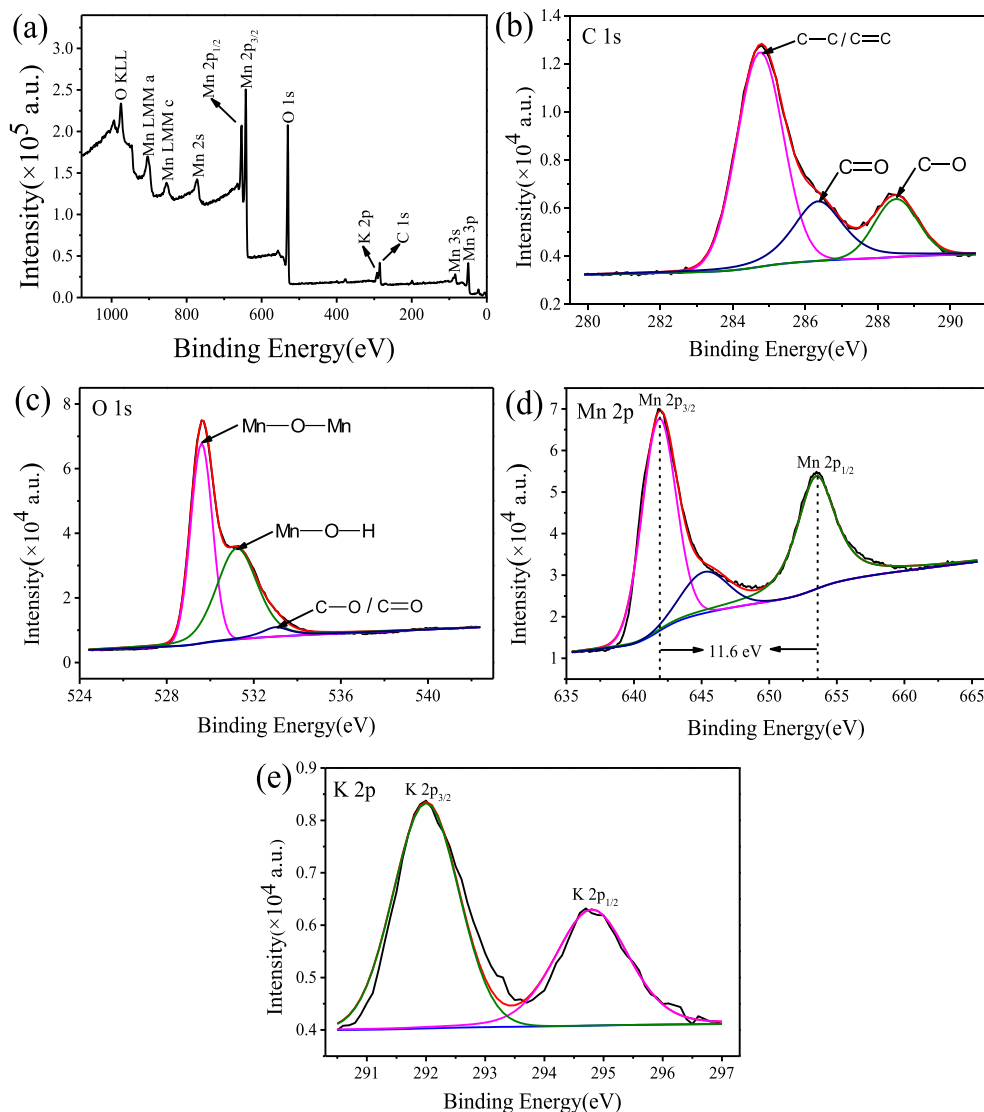


Fig. 2. XPS surveys of CMMO-8. (a) full survey, (b) C 1s region, (c) O 1s region, (d) Mn 2p region, and (e) K 2p region.

literature [15]. Moreover, it is worth noting that the K2p signal also exists in the survey (Fig. 2(d)) and the two main peaks around 292.0 and 294.8 eV can be attributed to K2p_{3/2} and K2p_{1/2}, respectively, indicating that some K⁺ reserved in the interlayers of MnO₂ [32].

The morphology and size of CMMO-X composites are characterized by SEM. As shown in Fig. 3, the structures of these samples varied from each other depending on the reaction times. The samples obtained in relative short time (e.g. 5 and 8 h) show nanoflower morphology with diameters of 1–3 μm and invaginated surface, and they inherit the initial morphology of the raw MC spheres. High-magnification picture displays that the nanoflowers are composed of many interconnected thin petals with smooth texture, and the thickness of each petal is about 15 nm. While, one can clearly observe the petals of CMMO-8 are denser than that of CMMO-5. Upon hydrothermal treatment for 10 h, the petals of the CMMO spheres show many fragments, and the morphology of the CMMO tends to smooth sphere. When the reaction time extends to 12 h, the composites turn into sea urchin-like structures consisting of numerous nanoneedles.

To illustrate the microstructure of MC and CMMO-X composites, TEM and HRTEM measurements were performed. Fig. 4(A) depicts

the TEM image of MC sphere, which clearly reveals the pores distributed throughout the sphere. After the reaction with KMnO₄ for 8 h, the CMMO spheres inherit the morphology of the MC substrates as shown in Fig. 4(B–D). Such a changing should be ascribed to the high efficient consumption of MC [32]. By close observation one can find that the nanoflowers are composed of many ultrathin nanoflakes as indicated in the cycle of Fig. 4(E). Furthermore, the high-resolution TEM image of CMMO-8 is described in Fig. 4(F). The lattice fringe can be observed with an interplanar distance of about 0.29 nm, which is corresponding to the (310) planes of α-MnO₂ structure and the value is in good accordance with the XRD result [40].

To understand the growth process of the CMMO spheres, the morphology, structure and composition of the samples at different reaction stages have been monitored with SEM, TEM and EDS measurements. After the mixing of MC with KMnO₄ aqueous solution and stirred for 2, 8 and 12 h at ambient temperature, the solids retrieved from the suspension at different reaction stages show quite similar morphology to pristine MC spheres (see images A, B and C of Fig. S1). Definitely, after the addition of H₂SO₄ aqueous solution to the suspension and stirred for further 2 h, the spheres show

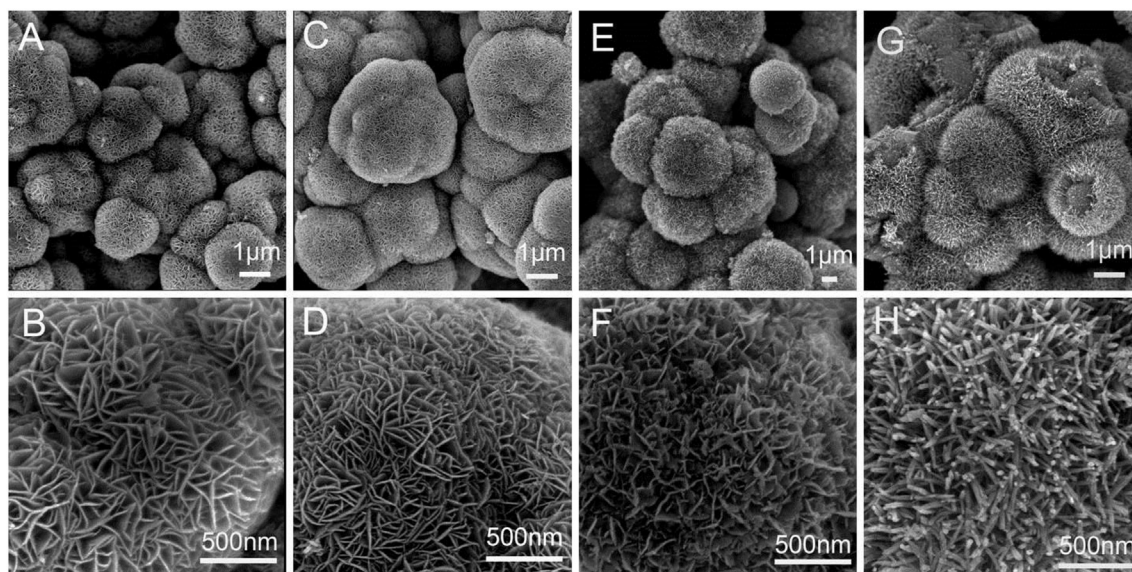


Fig. 3. FESEM images of CMMO-X composites prepared at 60 °C with different hydrothermal time: (A,B) CMMO-5, (C,D) CMMO-8, (E,F) CMMO-10, (G,H) CMMO-12, respectively.

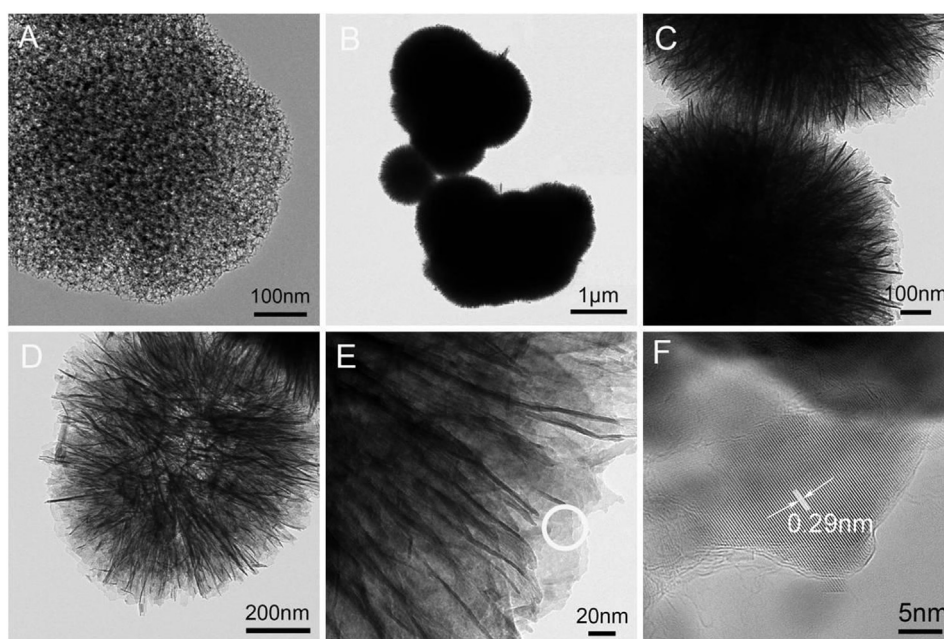


Fig. 4. TEM image of MC (A); TEM images (B–E) and HRTEM image (F) of CMMO-8 composite.

obviously a fluffy surface. To investigate the detailed structure evolution of the samples at different reaction stages, TEM measurements have been performed and the results are depicted in Fig. S2. From the images one can see clearly the porous structure, which is similar to that of the MC raw materials, even stirred with KMnO_4 aqueous solution for 12 h. Whereas, the sample structure changed dramatically after the addition of H_2SO_4 . When the suspension was stirred for further 2 h after the addition of H_2SO_4 , layered structure appeared in the spheres. Such a result can be explained as due to the enhancement of the oxidizability of KMnO_4 in the presence of H_2SO_4 , which then accelerated the redox reaction between KMnO_4 and amorphous carbon, forming sheet-structured MnO_2 at the expense of MC substrate. EDS element mapping measurements have also been carried out to roughly estimate the composition evolution of the

sample at different reaction stages. As can be seen from Fig. S3, the intensity of carbon signal faded obviously after the addition of H_2SO_4 for 2 h, on the contrary, the oxygen signal turned to dominate in the mapping. The EDS element mapping measurements are in accordance with the SEM and TEM results.

Fig. 5 shows the nitrogen adsorption-desorption isotherms and the corresponding pore size distributions of MC and CMMO-8 composite spheres. As can be seen in Fig. 5(a), a typical type-IV isotherm is obtained at relative pressure between 0.7 and 0.9, exhibiting obvious hysteresis loops and steep capillary condensation steps. This phenomenon indicates micropores and mesopores coexist in the MC [41]. The MC spheres display a high BET specific surface area of $757 \text{ m}^2 \text{ g}^{-1}$ and a pore volume of $1.56 \text{ cm}^3 \text{ g}^{-1}$. In comparison with MC spheres, the CMMO-8 composite shows an

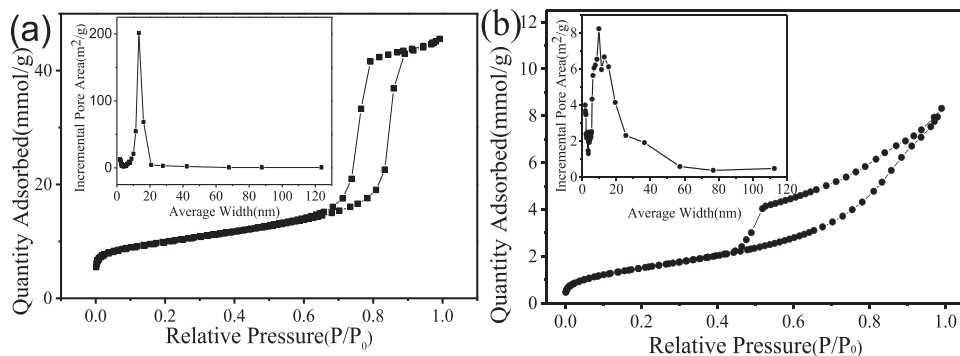


Fig. 5. The nitrogen adsorption–desorption isotherms and pore size distribution curves (inset) of as-synthesized MC (panel a) and CMMO-8 (panel b).

irregular type-IV isotherm as shown in Fig. 5(b). The specific surface area and pore volume decrease to $126 \text{ m}^2 \text{ g}^{-1}$ and $0.27 \text{ cm}^3 \text{ g}^{-1}$ respectively. Furthermore, it is obvious that the capillary condensation steps expand to the lower relative pressure, implying an increase of pore size. The specific surface area and pore volume of these samples are summarized in Table 1.

The electrochemical performance of CMMO-X was tested by cyclic voltammograms (CV) and galvanostatic charge/discharge (GCD) using a 2 mol/L KOH aqueous solution as electrolyte. In order to get a reliable performance, a two-electrode configuration was selected for the measurements [42]. Fig. 6(a) depicts the typical CV curves of the four as-synthesized samples at a scan rate of 50 mV s^{-1} with the voltage window of 0–0.8 V. It can be seen all of the CV curves remain nearly rectangular shape, indicating reversible electrochemical performance [43]. Further observation can be found that among the four samples, CMMO-8 owns the largest area than the three others, suggesting the superior specific capacitance. Fig. 6(b) shows the galvanostatic charge/discharge test of capacitors made from these CMMO-X samples at a current density of $0.5 \text{ A} \cdot \text{g}^{-1}$ with the working voltage window from 0 to 1 V. It is obvious that there's a slight IR drop in all curves, which can be attributed to the intrinsic resistance of MnO_2 [32], nevertheless the CMMO-X composites still maintain remarkable reversibility and conductivity. The specific capacitance of CMMO-X is calculated by the following equation: $C = 4I\Delta t / (m\Delta V)$, where m is the overall mass of the electroactive materials, I is the discharging current (A), Δt is the discharging time(s), and ΔV is the discharging potential range (V), respectively.

The specific capacitance of CMMO-X composites are calculated depending on several current densities and be exhibited in Fig. 6(c). It can be seen that CMMO-8 composite spheres show the highest specific capacitance among the four samples, and it demonstrates an average specific capacitance of 236 F g^{-1} at a current density of 10 A g^{-1} which retains 55% of the specific capacitance delivered at a current density of 0.3 A g^{-1} . In comparison with pristine MnO_2 reported in the literature, for example MnO_2 nanoflowers delivered a specific capacitance of 197.3 F g^{-1} at 1 A g^{-1} in $1 \text{ mol L}^{-1} \text{ Na}_2\text{SO}_4$ electrolyte [14], the three other CMMO samples possess also superior values of specific capacitance. It should also be mentioned that

the excellent specific capacitance of CMMO-8 surpasses dramatically the performance of many documented nanocomposites composing of MnO_2 and carbon-based materials, for instance the MnO_2 nanoflakes/HPCs nanocomposite displays a specific capacitance of 326.9 F g^{-1} [39], while the sea urchin-like RGO/ MnO_2 nanocomposite assembly exhibits a specific capacitance of 125.93 F g^{-1} at 1 A g^{-1} [44]. All of these evidences confirm that the capacitance and rate capability of CMMO-8 sample outperforms many other reported MnO_2 nanocomposites. The high performance of CMMO-8 can be ascribed to the following two factors. Firstly, the uniform pore structure and large specific surface area of the composite spheres provide plentiful contact area and active sites to facilitate the accessibility of electrolyte. Secondly, the vertically arranged thin petals or needles derived by sacrificing the MC spheres can shorten the transport route of ions in electrolyte, ensuring the reversible reaction between the electrolyte and active materials which then can enhancing greatly the specific capacitance [45].

To further understand the utility of as-synthesized CMMO-X composites, the Ragone plot was performed between the energy density and power density as been shown in Fig. 6(d). The values were calculated by the following two equations of (1) and (2):

$$E = CV^2 / 7.2 \quad (1)$$

$$P = 3600 \times E/t \quad (2)$$

From the curves it can be seen that the energy density decreases with the increase of power density. It is obvious that the energy densities of the four samples are higher than the traditional capacitors, and the power densities are superior even than that of batteries [46]. Particularly, the CMMO-8 composite spheres possess a large energy density of $8.9 \text{ Wh} \cdot \text{kg}^{-1}$ and a high power density of 3500 W kg^{-1} . All these evidences indicate that the CMMO-X composites are ideally candidates for pseudocapacitors.

The electrochemical performance of MC and CMMO-8 has been further investigated and compared in details and their CV profiles at scan rate from 5 to 100 mV s^{-1} have been depicted in Fig. 7 as panels (a) and (b), respectively. All these curves for MC remain symmetric rectangular shape as scan rate increased, indicating typical double-layer capacitor properties. The high reversibility can be ascribed to the uniform pore structures and excellent conductivity of MC spheres. While, the CV profiles for CMMO-8 exhibit relatively rectangular shape especially at low scan rates of 5, 10, 30 and 50 mV s^{-1} , declaring reversible performance. However, when the scan rate increase to 80 and 100 mV s^{-1} the CV curves deviate from rectangular. This should be attributed to the polarization on account of the transport resistance [15]. It is worth noting that these CV curves still remain symmetric shape, indicating obviously Faradic reactions and excellent electrochemical performance. To evaluate further the

Table 1
BET specific surface area and pore volume of CMMO-X.

Sample	BET Surface area ($\text{m}^2 \cdot \text{g}^{-1}$)	Pore Volume ($\text{m}^3 \text{ g}^{-1}$)
CMMO-5	68.7	0.20
CMMO-8	126.2	0.27
CMMO-10	123.1	0.32
CMMO-12	87.9	0.25

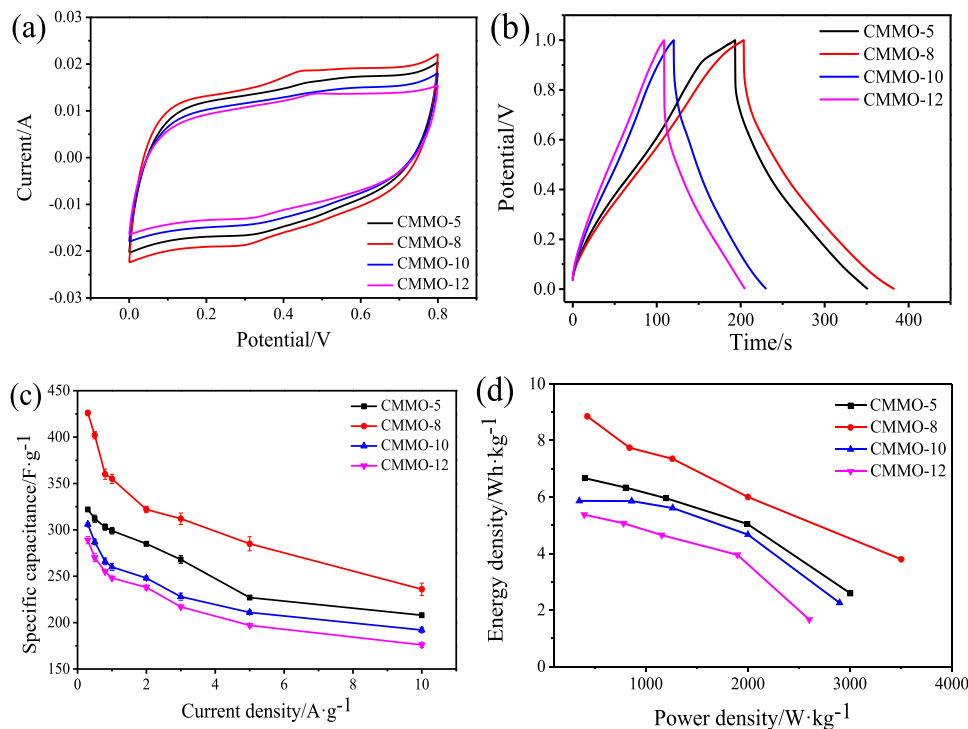


Fig. 6. Electrochemical performance of CMMO-X: (a) CV curves at a scan rate of 50 mV/s; (b) GCD curves at a current density of 0.5 A g^{-1} ; (c) Comparison of specific capacitances of these CMMO-X spheres depending on the current density (the error bars were deduced from triplicated measurements); (d) Ragone plots of CMMO-X.

performance of MC and CMMO-8 more efficiently, the galvanostatic charge-discharge performance has been carried out at different current density from 0.3 to 10 A g^{-1} . Fig. 7(c) gives out the specific galvanostatic charge-discharge performance of MC electrode. The curves are normal triangle shapes, exhibiting good coulombic efficiency and ideal double-layer capacitor behaviors. Fig. 7(d) shows the specific galvanostatic charge-discharge performance of CMMO-8 electrode. It can be seen that the curves are nearly linear and symmetric with the increase of current density. Furthermore, by examining the curves carefully one can found that the IR drop increases along with the increasing of current density. It can be ascribed to the higher current density, which quickens the charge-discharge process and results in the un-sufficient contact between ions and active materials [14]. The specific capacitances of MC and CMMO-8 have been presented in Fig. 7(e). It can be seen that the composite electrode surpasses the MC one dramatically. However the rate capability of MC is better than the composite. The electrochemical impedance spectroscopy (EIS) for MC and CMMO-8 have been compared in Fig. 7 as panel (f). The Nyquist plot can be divided into two regions: high frequency region with a semicircle and low frequency region with a Warburg tail. The intersection of the curve with x-axis represents inner resistance (R_s), which including the intrinsic resistance of active material, the electrolyte resistance, and the interface resistance between active material and current collector. The diameter of the semicircle means the charge transfer resistance (R_{ct}). The straight line represents the diffusion resistance of ions. As can be seen, the R_s of these two samples are of 0.7 and 0.9Ω , and the R_{ct} are of 1 and 2.3Ω , respectively. Obviously, the MC possesses higher conductivity than CMMO-8 since the former shows a smaller semicircle and a more vertical line in the low frequency region [47]. However, it's worth noting that the resistance of CMMO-8 composite is lower than many other materials. Thus, the CMMO composites can be considered as promising materials in the application of supercapacitors.

Furthermore, the cycle stability of CMMO-8 electrode is investigated by galvanostatic charge/discharge test at a current density of 1.0 A g^{-1} for 5000 cycles, and the corresponding specific capacitance has been depicted in Fig. 8. As can be seen, in the first 100 cycles, the specific capacitance of CMMO-8 electrode decreased only about 2.6%. In the following 400 cycles, the specific capacitance has a dramatically decay with a decreasing ratio of about 12.1% compared with the first cycle. Afterwards, the specific capacitance of CMMO-8 electrode decreased only about 10.3% in the following 3500 cycles. Though, the CMMO-8 electrode only delivers 75% retention of the initial performance after 5000 cycles, it still possesses a high specific capacitance of 258 F/g , which is higher than that of MC and pristine MnO_2 . Therefore, the CMMO composites possess a promising practical importance [48].

4. Conclusions

In general, CMMO composites with novel nanoflower or sea urchin-like nanostructure have been prepared by a low temperature hydrothermal method using mesoporous carbon spheres as reductive agent and consuming template. The mesoporous carbon spheres with uniform pore size distribution were prepared by a spray-drying assisted hard template method using biomass as precursor, which were then consumed by reacting with KMnO_4 . The morphology of the CMMO composite spheres can be modified from flower-like to sea urchin-like by simply tuning the hydrothermal treating time. The formation mechanism of the MnO_2 is directed to the in-situ reaction between the KMnO_4 and mesoporous carbon with the assistance of H_2SO_4 . The obtained CMMO composites with carbon content in range of 3–4 wt% were used as electrode materials for supercapacitors and they exhibit superior rate capability and long cycling performance in a 2 mol L^{-1} KOH aqueous solution electrolyte. The excellent performances of the CMMO composites are attributed on the one hand to the

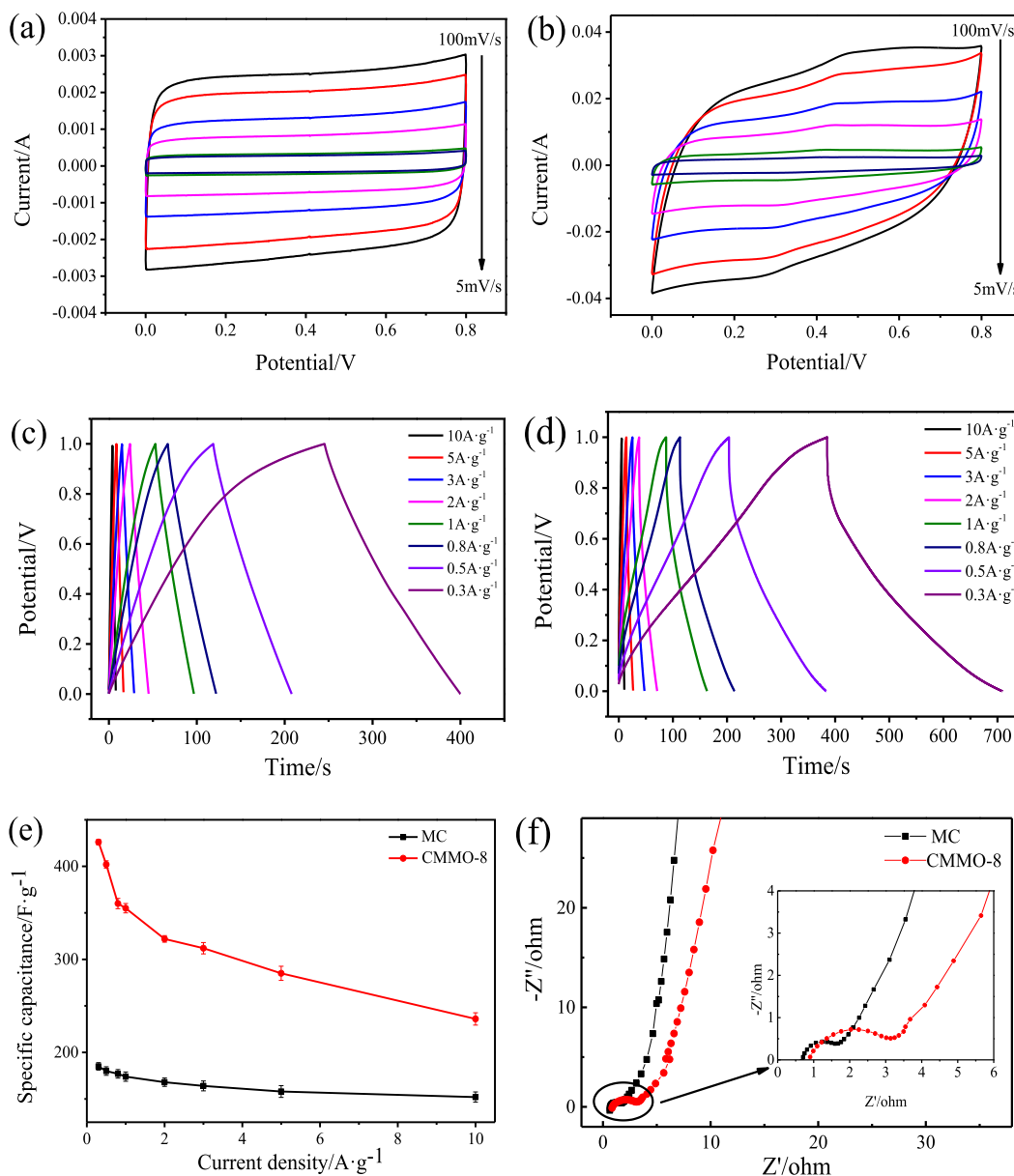


Fig. 7. Cyclic voltammograms of (a) MC, and (b) CMMO-8 at various scan rates from 5 to 100 mV s^{-1} ; galvanostatic charge/discharge profiles of (c) MC spheres, and (d) CMMO-8 at various current densities from 0.3 to 10 A g^{-1} ; (e) corresponding specific capacitance of MC and CMMO-8 depending on different current densities; (f) comparison of Nyquist plots between MC and CMMO-8.

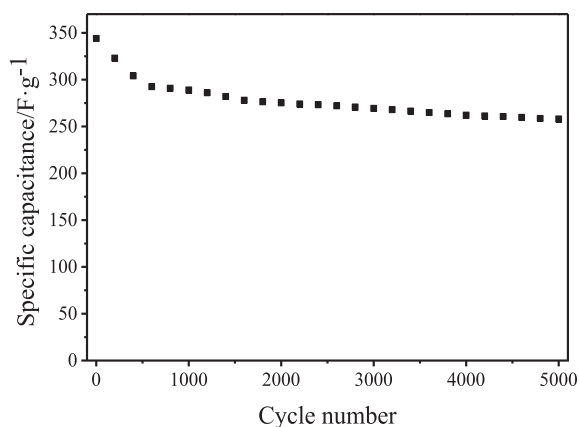


Fig. 8. Long cycling stability of CMMO-8 composite electrode at a current density of 1.0 A g^{-1} for 5000 cycles.

combination of high specific capacitance of MnO_2 with the good conductivity of residual carbon substrates, and on the other hand to the vertically arranged petals or needles in the CMMO spheres, which is of benefit to the penetration of electrolyte. It is obvious that the CMMO composite is a kind of potential material for practical application in supercapacitors. Meanwhile, the preparation route developed in this work will also provide some enlightenment for the synthesis of other hybrid materials.

Acknowledgements

This work is supported by the National Key Project on Basic Research (Grant No 2012CB722705) and the National High Technology Research and Development Program (NO. 2014AA250323) of China. We acknowledge the Taishan Scholars Advantageous and Distinctive Discipline Program of Shandong Province for supporting the research team of energy storage materials. Y. Wang would like

to thank the financial support from the Top-notch Innovative Talent Program of Qingdao City (Grant no.: 13-CX-8). Y. Li thanks the Taishan Scholar Program of Shandong Province (201511029).

Appendix A. Supplementary data

Supplementary data related to this article can be found at <http://dx.doi.org/10.1016/j.jallcom.2017.05.035>.

References

- [1] K. Wang, S. Gao, Z. Du, A. Yuan, W. Lu, L. Chen, MnO₂-Carbon nanotube composite for high-areal-density supercapacitors with high rate performance, *J. Power Sources* 305 (2016) 30–36.
- [2] N. Jabeen, Q. Xia, M. Yang, H. Xia, Unique core-shell nanorod arrays with polyaniline deposited into mesoporous NiCo₂O₄ support for high-performance supercapacitor electrodes, *ACS Appl. Mater. Interfaces* 8 (2016) 6093–6100.
- [3] P. Guo, Y. Gu, Z. Lei, Y. Cui, X.S. Zhao, Preparation of sucrose-based microporous carbons and their application as electrode materials for supercapacitors, *Microporous Mesoporous Mater.* 156 (2012) 176–180.
- [4] T. Gu, B. Wei, Fast and stable redox reactions of MnO₂/CNT hybrid electrodes for dynamically stretchable pseudocapacitors, *Nanoscale* 7 (2015) 11626–11632.
- [5] Y. Zhao, C.-A. Wang, Extremely facile synthesis of manganese dioxide-polyaniline nano-reticulation with enhanced electrochemical properties, *J. Alloys Compd.* 677 (2016) 281–287.
- [6] Y. Yu, Y. Zhai, H. Liu, L. Li, Single-layer MnO₂ nanosheets: from controllable synthesis to free-standing film for flexible supercapacitors, *Mater. Lett.* 176 (2016) 33–37.
- [7] J. Jiang, W. Shi, S. Song, Q. Hao, W. Fan, X. Xia, X. Zhang, Q. Wang, C. Liu, D. Yan, Solvothermal synthesis and electrochemical performance in super-capacitors of Co₃O₄/C flower-like nanostructures, *J. Power Sources* 248 (2014) 1281–1289.
- [8] C. Xiong, T. Li, A. Dang, T. Zhao, H. Li, H. Lv, C. Xiong, T. Li, A. Dang, T. Zhao, Two-step approach of fabrication of three-dimensional MnO₂-graphene-carbon nanotube hybrid as a binder-free supercapacitor electrode, *Rsc Adv.* 5 (2016) 602–610.
- [9] Z. Yu, L. Tetaud, L. Zhai, J. Thomas, Supercapacitor electrode materials: nanostructures from 0 to 3 dimensions, *Energy Environ. Sci.* 8 (2015) 702–730.
- [10] X. Zhang, X. Meng, S. Gong, P. Li, L.E. Jin, Q. Cao, Synthesis and characterization of 3D MnO₂/carbon microtube bundle for supercapacitor electrodes, *Mater. Lett.* 179 (2016) 73–77.
- [11] K.S. Yang, B.-H. Kim, Highly conductive, porous RuO₂/activated carbon nanofiber composites containing graphene for electrochemical capacitor electrodes, *Electrochim. Acta* 186 (2015) 337–344.
- [12] L.L. Zhang, X.S. Zhao, Carbon-based materials as supercapacitor electrodes, *Chem. Soc. Rev.* 38 (2009) 2520–2531.
- [13] M. Kim, Y. Kim, K.M. Lee, S.Y. Jeong, E. Lee, S.H. Baek, E.S. Sang, Electrochemical improvement due to alignment of carbon nanofibers fabricated by electrospinning as an electrode for supercapacitor, *Carbon* 99 (2015) 607–618.
- [14] S. Zhao, T. Liu, D. Hou, W. Zeng, B. Miao, S. Hussain, X. Peng, M.S. Javed, Controlled synthesis of hierarchical birnessite-type MnO₂ nanoflowers for supercapacitor applications, *Appl. Surf. Sci.* 356 (2015) 259–265.
- [15] X. Wang, X. Fan, G. Li, M. Li, X. Xiao, A. Yu, Z. Chen, Composites of MnO₂ nanocrystals and partially graphitized hierarchically porous carbon spheres with improved rate capability for high-performance supercapacitors, *Carbon* 93 (2015) 258–265.
- [16] Z. Lei, F. Shi, L. Lu, Incorporation of MnO₂-coated carbon nanotubes between graphene sheets as supercapacitor electrode, *ACS Appl. Mater. Interfaces* 4 (2012) 1058–1064.
- [17] X.-Y. Zhang, L.-Q. Han, S. Sun, C.-Y. Wang, M.-M. Chen, MnO₂/C composite electrodes free of conductive enhancer for supercapacitors, *J. Alloys Compd.* 653 (2015) 539–545.
- [18] Y. Zhao, C.-A. Wang, Nano-network MnO₂/polyaniline composites with enhanced electrochemical properties for supercapacitors, *Mater. Des.* 97 (2016) 512–518.
- [19] P. Guo, Z. Li, S. Liu, J. Xue, G. Wu, H. Li, X.S. Zhao, Electrochemical properties of colloidal nanocrystal assemblies of manganese ferrite as the electrode materials for supercapacitors, *J. Mater. Sci.* 52 (2017) 5359–5365.
- [20] L. Jing, A. Fu, H. Li, J. Liu, P. Guo, Y. Wang, X.S. Zhao, One-step solvothermal preparation of Fe₃O₄/graphene composites at elevated temperature and their application as anode materials for lithium-ion batteries, *RSC Adv.* 4 (2014) 59981–59989.
- [21] H.R. Naderi, P. Norouzi, M.R. Ganjali, Electrochemical study of a novel high performance supercapacitor based on MnO₂/nitrogen-doped graphene nanocomposite, *Appl. Surf. Sci.* 366 (2016) 552–560.
- [22] X. Zhang, P. Yu, H. Zhang, D. Zhang, X. Sun, Y. Ma, Rapid hydrothermal synthesis of hierarchical nanostructures assembled from ultrathin birnessite-type MnO₂ nanosheets for supercapacitor applications, *Electrochim. Acta* 89 (2013) 523–529.
- [23] I.-T. Kim, N. Kouda, N. Yoshimoto, M. Morita, Preparation and electrochemical analysis of electrodeposited MnO₂/C composite for advanced capacitor electrode, *J. Power Sources* 298 (2015) 123–129.
- [24] X.L. Guo, M. Kuang, F. Dong, Y.X. Zhang, Monodispersed plum candy-like MnO₂ nanosheets-decorated NiO nanostructures for supercapacitors, *Ceram. Int.* 42 (2016) 7787–7792.
- [25] X. Feng, Z. Yan, N. Chen, Y. Zhang, Y. Ma, X. Liu, Q. Fan, L. Wang, W. Huang, The synthesis of shape-controlled MnO₂/graphene composites via a facile one-step hydrothermal method and their application in supercapacitors, *J. Mater. Chem. A* 1 (2013) 12818–12825.
- [26] Z. Wang, F. Wang, J. Tu, D. Cao, X. An, Y. Ye, Nickel foam supported hierarchical mesoporous MnO₂/Ni(OH)₂ nanosheet networks for high performance supercapacitor electrode, *Mater. Lett.* 171 (2016) 10–13.
- [27] A. Bello, O.O. Fashedemi, F. Barzegar, M.J. Madito, D.Y. Momodu, T.M. Masikhwa, J.K. Dangbegnon, N. Manyala, Microwave synthesis: characterization and electrochemical properties of amorphous activated carbon-MnO₂ nanocomposite electrodes, *J. Alloys Compd.* 681 (2016) 293–300.
- [28] Z. Lei, J. Zhang, X.S. Zhao, Ultrathin MnO₂ nanofibers grown on graphitic carbon spheres as high-performance asymmetric supercapacitor electrodes, *J. Mater. Chem.* 22 (2012) 153–160.
- [29] S. Kong, K. Cheng, Y. Gao, T. Ouyang, K. Ye, G. Wang, D. Cao, A novel three-dimensional manganese dioxide electrode for high performance supercapacitors, *J. Power Sources* 308 (2016) 141–148.
- [30] N. Zhang, P. Qi, Y.-H. Ding, C.-J. Huang, J.-Y. Zhang, Y.-Z. Fang, A novel reduction synthesis of the graphene/Mn₃O₄ nanocomposite for supercapacitors, *J. Solid State Chem.* 237 (2016) 378–384.
- [31] J. Zhang, H. Li, P. Guo, H. Ma, X.S. Zhao, Rational design of graphitic carbon based nanostructures for advanced electrocatalysis, *J. Mater. Chem. A* 4 (2016) 8497–8511.
- [32] J. Liu, Y. Zhang, Y. Li, J. Li, Z. Chen, H. Feng, J. Li, J. Jiang, D. Qian, In situ chemical synthesis of sandwich-structured MnO₂/graphene nanoflowers and their supercapacitive behavior, *Electrochim. Acta* 173 (2015) 148–155.
- [33] S.K. Park, D.H. Suh, H.S. Park, Electrochemical assembly of reduced graphene oxide/manganese dioxide nanocomposites into hierarchical sea urchin-like structures for supercapacitive electrodes, *J. Alloys Compd.* 668 (2016) 146–151.
- [34] S. Lu, D. Yan, L. Chen, G. Zhu, H. Xu, A. Yu, One-pot fabrication of hierarchical Ag/MnO₂ nanoflowers for electrochemical capacitor electrodes, *Mater. Lett.* 168 (2016) 40–43.
- [35] Y. Zhang, C. Zhang, G. Huang, B. Xing, Y. Duan, Synthesis and capacitive properties of manganese oxide nanoparticles dispersed on hierarchical porous carbons, *Electrochim. Acta* 166 (2015) 107–116.
- [36] D. Wang, A. Fu, H. Li, Y. Wang, J. Liu, P. Guo, X.S. Zhao, Mesoporous carbon spheres with controlled porosity for high-performance lithium-sulfur batteries, *J. Power Sources* 285 (2015) 469–477.
- [37] M. Leżańska, A. Olejniczak, A. Pacuta, G. Szymański, J. Wtoch, The influence of microporosity creation in highly mesoporous N-containing carbons obtained from chitosan on their catalytic and electrochemical properties, *Catal. Today* 227 (2014) 223–232.
- [38] J. Qu, L. Shi, C. He, F. Gao, B. Li, Q. Zhou, H. Hu, G. Shao, X. Wang, J. Qiu, Highly efficient synthesis of graphene/MnO₂ hybrids and their application for ultrafast oxidative decomposition of methylene blue, *Carbon* 66 (2014) 485–492.
- [39] H. Li, L. Jiang, Q. Cheng, Y. He, V. Pavlinek, P. Saha, C. Li, MnO₂ nanoflakes/hierarchical porous carbon nanocomposites for high-performance supercapacitor electrodes, *Electrochim. Acta* 164 (2015) 252–259.
- [40] W. Ma, S. Chen, S. Yang, W. Chen, Y. Cheng, Y. Guo, S. Peng, S. Ramakrishna, M. Zhu, Hierarchical MnO₂ nanowire/graphene hybrid fibers with excellent electrochemical performance for flexible solid-state supercapacitors, *J. Power Sources* 306 (2016) 481–488.
- [41] H. Li, H. Liu, A. Fu, G. Wu, M. Xu, G. Pang, P. Guo, J. Liu, X.S. Zhao, Synthesis and characterization of N-doped porous TiO₂ hollow spheres and their photocatalytic and optical properties, *Materials* 9 (2016) 849.
- [42] M.D. Stoller, R.S. Ruoff, Best practice methods for determining an electrode material's performance for ultracapacitors, *Energy Environ. Sci.* 3 (2010) 1294–1301.
- [43] D. Zhu, Y. Wang, G. Yuan, H. Xia, High-performance supercapacitor electrodes based on hierarchical Ti/MnO₂ nanowire arrays, *Chem. Commun.* 50 (2014) 2876–2878.
- [44] S.K. Park, D.H. Suh, H.S. Park, Electrochemical assembly of reduced graphene oxide/manganese dioxide nanocomposites into hierarchical sea urchin-like structures for supercapacitive electrodes, *J. Alloys Compd.* 668 (2016) 146–151.
- [45] H. Xia, C. Hong, X. Shi, B. Li, G. Yuan, Q. Yao, J. Xie, Hierarchical heterostructures of Ag nanoparticles decorated MnO₂ nanowires as promising electrodes for supercapacitors, *J. Mater. Chem. A* 3 (2015) 1216–1221.
- [46] N.R. Chodankar, D.P. Dubal, G.S. Gund, C.D. Lokhande, Flexible all-solid-state MnO₂ thin films based symmetric supercapacitors, *Electrochim. Acta* 165 (2015) 338–347.
- [47] H. Xia, D. Zhu, Z. Luo, Y. Yu, X. Shi, G. Yuan, J. Xie, Hierarchically structured Co₃O₄@Pt/MnO₂ nanowire arrays for high-performance supercapacitors, *Sci. Rep.* 3 (2013) 2978.
- [48] H.Z. Chi, H. Zhu, L. Gao, Boron-doped MnO₂/carbon fiber composite electrode for supercapacitor, *J. Alloys Compd.* 645 (2015) 199–205.